IPEM Institute of Physics and Engineering in Medicine

NOTE

# A detector's eye view (DEV)-based OSEM algorithm for benchtop x-ray fluorescence computed tomography (XFCT) image reconstruction

View the article online for updates and enhancements.

# Physics in Medicine & Biology

IPEM Institute of Physics and Engineering in Medicine

**NOTE**

# A detector's eye view (DEV)-based OSEM algorithm for benchtop x-ray fluorescence computed tomography (XFCT) image reconstruction

**Luzhen Deng**[1,2]**, Md F Ahmed**[1]**, Sandun Jayarathna**[1]**, Peng Feng**[2]**, Biao Wei**[2] **and Sang Hyun Cho**[1,3,4]

[1] Department of Radiation Physics, The University of Texas MD Anderson Cancer Center, Houston, TX, United States of America
[2] Key Laboratory of Optoelectronics Technology and System, Chongqing University, Ministry of Education, Chongqing 400044, People's Republic of China
[3] Department of Imaging Physics, The University of Texas MD Anderson Cancer Center, Houston, TX 77030, United States of America
[4] Author to whom correspondence may be addressed.

E-mail: scho@mdanderson.org

## Abstract

In this study, we developed a detector's eye view (DEV)-based ordered subsets expectation maximization (OSEM) algorithm for more accurate reconstruction of benchtop x-ray fluorescence computed tomography (XFCT) images. The proposed approach was tested using two sets of benchtop XFCT imaging data derived from a newly performed gold nanoparticle (GNP)-containing phantom imaging study and a previously published postmortem benchtop XFCT imaging study of a tumor-bearing mouse injected with GNPs. DEV-based OSEM resulted in higher spatial resolution (up to ~20% decrease in the full width at half maximum values of the regions of interest), compared with filtered back-projection (FBP) and traditional OSEM. It also resulted in up to an order of magnitude smaller background noise in the reconstructed images than FBP, while producing consistently less background noise than traditional OSEM.

## 1. Introduction

X-ray fluorescence (XRF) analysis is a highly sensitive technique capable of quantifying and identifying an element of interest such as gold by detecting XRF photons emitted from the element (Cesareo and Viezzoli 1983, Pushie *et al* 2014). XRF analysis can be combined with computed tomography (CT) to create a powerful spectroscopic/quantitative x-ray imaging modality known as x-ray fluorescence computed tomography (XFCT), traditionally associated with synchrotron x-ray sources (Cesareo and Mascarenhas 1989, Rust and Weigelt 1998). Benchtop XFCT setups implemented with polychromatic diagnostic x-ray sources (Cheong *et al* 2010, Jones *et al* 2012, Kuang *et al* 2013) have been proposed to image metal probes such as gold nanoparticles (GNPs), since these setups can offer a number of benefits such as easy access and low-cost instrumentation and operation.

Filtered back-projection (FBP) (Kak and Slaney 1988, Hsieh 2003) (one of analytic reconstruction algorithms), based on the inverse Radon transform, has been widely used for XFCT image reconstruction because of its simplicity. Since physical models require far more complexity than is expressed by a collection of line integrals, FBP may not yield accurate images, especially in terms of spatial resolution. Thus, iterative reconstruction methods, such as maximum-likelihood expectation maximization (Shepp and Vardi 1982, Lange and Carson 1984, Jones and Cho 2011) and its accelerated version, ordered subsets expectation maximization (OSEM) (Hudson and Larkin 1994), in which repeated applications of projection and back-projection are used to approximate the image that best fits the measurements, can alternatively be considered for XFCT image reconstruction. The methods to model the projection and back-projection (or build system matrix) in iterative reconstruction algorithms affect the reconstruction results considerably. Traditionally, for benchtop XFCT utilizing a cone-beam x-ray source, parallel-hole (or individual pin-hole) collimation is used to avoid detecting the XRF signal produced outside of the detection line of each detector element (or crystal). Under this condition, the system matrix is typically built by considering only the XRF signal reaching a detector element in question through a corre-
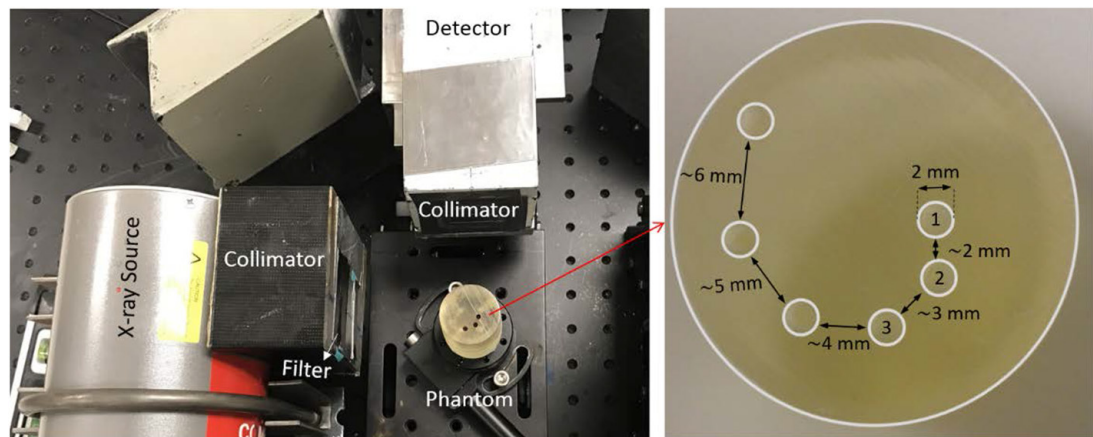
**Figure 1.** Top view of the current experimental benchtop XFCT system and the 3D printed PMMA phantom. As shown, the PMMA phantom has six spirally placed columns for various concentrations of GNP soulutions.

sponding pin-hole collimation (Jones and Cho 2011). In practice, however, the XRF signal originating from the same location within the imaging object could also be seen by neighboring detector elements. Hence, for accurate estimation of projection, the detector's eye view (DEV) through each pin-hole within a parallel-hole collimator should be considered in the system matrix.

To address the issue described previously, we developed a DEV-based OSEM method and tested it for benchtop XFCT image reconstruction, in comparison with FBP and traditional OSEM methods. We anticipate the currently proposed method will further advance benchtop XFCT imaging techniques, especially in preparation for routine *in vivo* imaging applications with an optimized benchtop XFCT setup adopting array or pixelated detectors.

## 2. Materials and methods

### 2.1. Benchtop XFCT imaging data

Two sets of benchtop XFCT imaging data were used for this study. Specifically, the first set of data was obtained from a newly performed benchtop XFCT imaging of a custom-made cylindrically shaped 3D-printed polymethyl methacrylate (PMMA) phantom (3 cm in diameter, 7 cm in height) containing six spirally placed columns (2 mm in diameter) that could be filled with GNP solutions (figure 1). The first three closest columns (labeled 1, 2, and 3 in a clockwise direction, as shown in figure 1) were loaded with 0.5 wt. % GNP solution prepared from commercially available GNPs (AuroVist 15 nm; Nanoprobes, Inc.). An experimental benchtop cone-beam XFCT system, as reported elsewhere (Manohar *et al* 2018), was used for the phantom imaging work. The second set of data was derived from a previously published postmortem benchtop XFCT imaging study of a tumor-bearing mouse injected with GNPs (Manohar *et al* 2016), which was performed by the current corresponding author's research group. Among the benchtop XFCT data available from this published work, those for the kidneys (corresponding CT images shown in figure 2) were found suitable for the current study. Although performed with different benchtop XFCT systems, both postmortem animal and phantom imaging studies were conducted by using the same x-ray tube voltage (125 kVp) with similar filtration (~2 mm of tin) and tube current (25 mA and 24 mA for the postmortem animal and phantom imaging, respectively). A dedicated high power x-ray source (MXR-160/22, COMET Technologies USA, Inc.) was used for the phantom imaging study, whereas a clinical orthovoltage x-ray unit (RT-250; Philips Healthcare, Inc.) was used for the postmortem animal imaging study. Both studies utilized the same x-ray detector and rotational stage: a thermoelectrically cooled cadmium telluride (CdTe) x-ray detector with the crystal size of 5 mm × 5 mm × 1 mm (AXR-CdTe, Amptek, Inc.) that provides the energy resolution of approximately 0.7 keV full width at half-maximum (FWHM) at the gold $K_\alpha$ XRF peaks (67–69 keV); a rotational stage (CR1-Z7, ThorLabs, Inc.) with a minimum incremental motion of 2.19 arcsec.

Benchtop XFCT data for the PMMA phantom containing GNP-loaded columns and the kidney slice of a mouse injected with GNPs were acquired with 60 (6° increment each) and 30 (12° increment each) projections, respectively. At each projection (or rotation), the CdTe detector located perpendicularly to the beam axis was translated 29 times (i.e. 30 translational positions) with a 1 mm step size for the PMMA phantom scan; the detector was translated 10 times (i.e. 11 translational positions) with a 3 mm step size for the mouse kidney scan. Such translations were necessary to mimic an array detector necessary to cover the entire imaging object, as described in detail elsewhere (Manohar *et al* 2016, 2018). A stainless steel collimator (with a 1 mm-diameter and 2.5 cm-thick aperture) and a lead collimator (with a 2.5 mm-diameter and 4 cm-thick aperture) were coupled with the CdTe detector for PMMA phantom and mouse kidney scans, respectively.
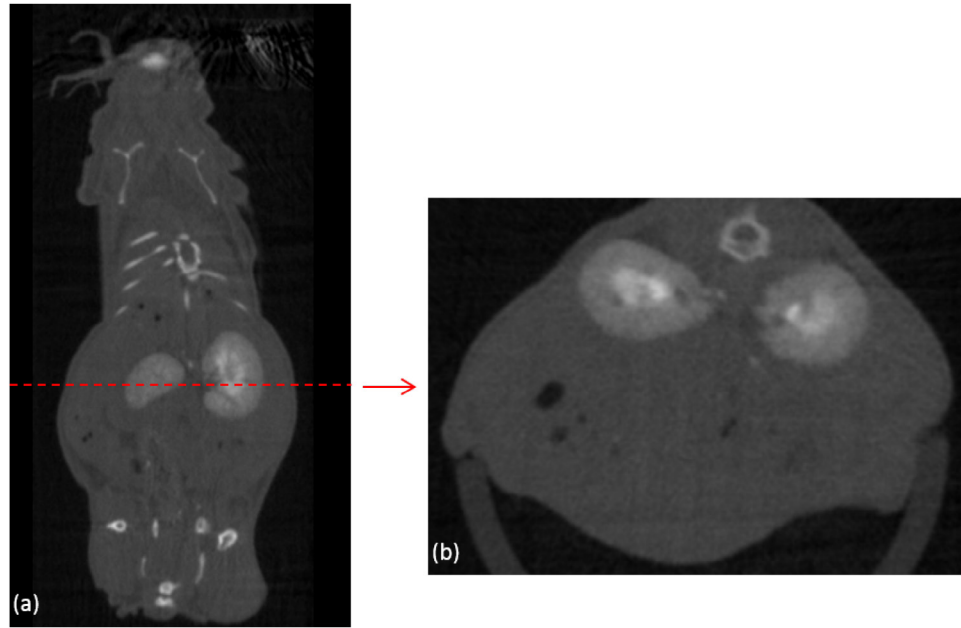
**Figure 2.** (a) Coronal CT slice of a postmortem mouse at 15 min after injection of GNPs. (b) Axial CT slice along the dotted line (kidneys). The current CT images were obtained from a previously published study (Manohar *et al* 2016) by the current corresponding author's group but not presented previously.

## 2.2. Reconstruction method

With use of the data set described in the preceding section, an image of the GNP distribution inside the phantom was reconstructed by applying an OSEM iterative reconstruction algorithm (Hudson and Larkin 1994). Since the ground truth about the dimension and shape of GNP-loaded columns within the PMMA phantom were known, the phantom results served to validate the proposed DEV-based OSEM algorithm. Subsequently, the proposed algorithm was applied to the mouse kidney case to test its effectiveness for realistic preclinical benchtop XFCT imaging.
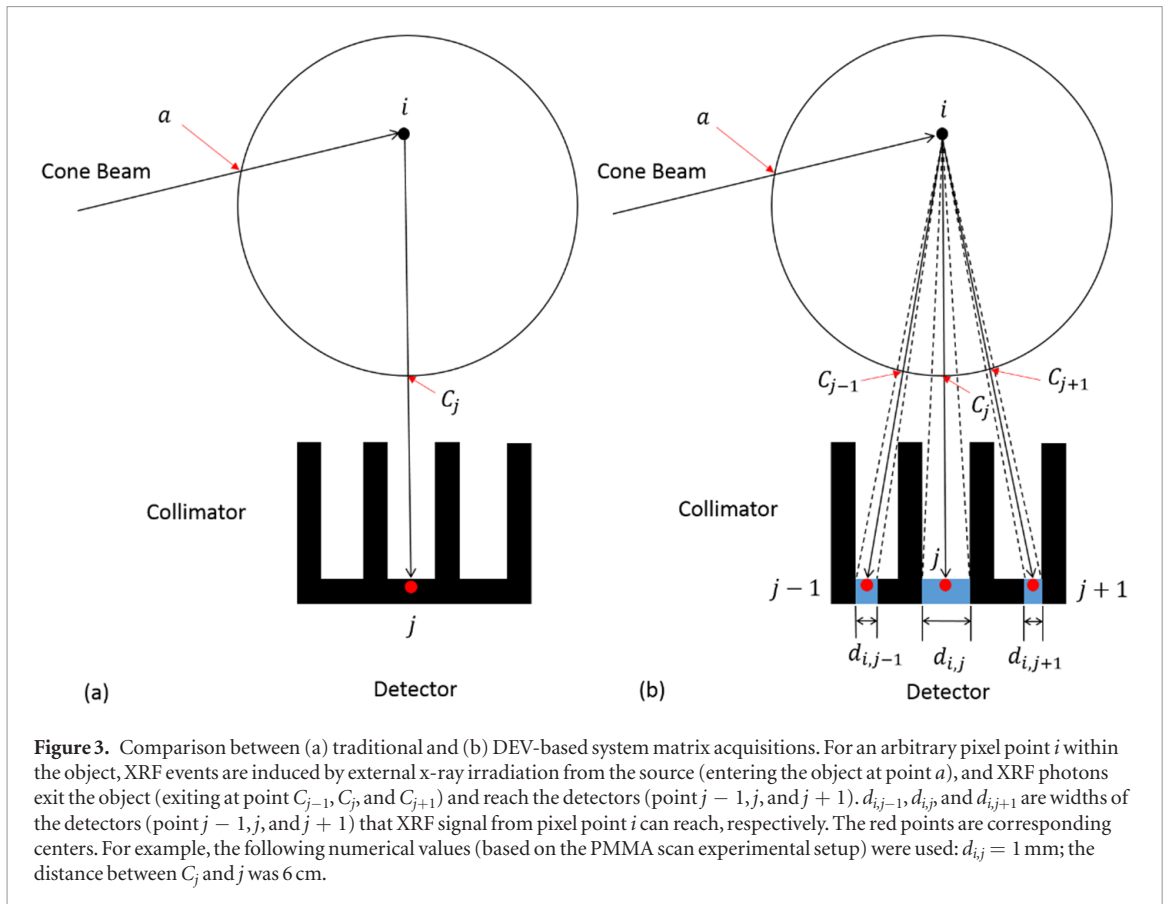
Consider a set of measured sinograms (or projection data set), $p$. Each element $p_j$ describes the gold XRF signal seen by one detector at a specific projection angle, and the number of elements in $p$ is equal to the product of the number of detectors and the number of projection angles. $p$ could be divided into $N$ subsets ($N = 2$ in the current study), and the subscript set of projection elements in the $n$th subset is $S_n$. We assume that $f$ is the reconstructed image, whose element $f_i$ represents the intensity of each pixel. The relationship between $p_j$ and $f_i$ is shown in equation (1), which is solved by equation (2) iteratively ($m > N$ is the iteration index, $S_m = S_N$ when $m$ is divided exactly by $N$, otherwise $S_m = S_{remainder((m+N)/N)}$) to get $f_i$ (Hudson and Larkin 1994):

$$p_j = \sum_i M_{i,j} f_i \tag{1}$$

$$f_i^{m+1} = \frac{f_i^m}{\sum_{j \in S_m} M_{i,j}} \times \sum_{j \in S_m} M_{i,j} \frac{p_j}{\sum_i M_{i,j} f_i^m} \tag{2}$$

where $M_{i,j}$ is the probability that an XRF photon will be created at pixel $f_i$ and detected in the projection element $p_j$. $M_{i,j}$ is the element of system matrix $M$ whose construction is critical for reconstruction. As shown in figure 3(a), traditionally, we assume that each detector (or detector element) could detect XRF photons from pixels only along the axis of each detector collimator, which means XRF photons emitted at pixel point $i$ could be detected only by detector $j$. In practice, however, the XRF signal originating from the same location within the imaging object could also be seen by neighboring detectors, which means the XRF signal from pixel point $i$ could also be detected by detectors $j - 1$ and $j + 1$. As shown in figure 3(b), $d_{i,j-1}$, $d_{i,j}$, and $d_{i,j+1}$, are widths of detectors ($j - 1$, $j$, and $j + 1$), respectively, that XRF signal from pixel point $i$ could reach. Realistic DEV of XRF photons and attenuation correction were considered in this study, and, consequently, the relationship proposed previously (Jones and Cho 2011) could be modified as:

$$M_{i,j} = \left(\frac{d_{i,j}}{|ij|}\right)^2 \exp\left(-\int_a^i \mu_{beam}(l_1) dl_1\right) \exp\left(-\int_i^{C_j} \mu_{gold}(l_{ij}) dl_{ij}\right) \tag{3}$$
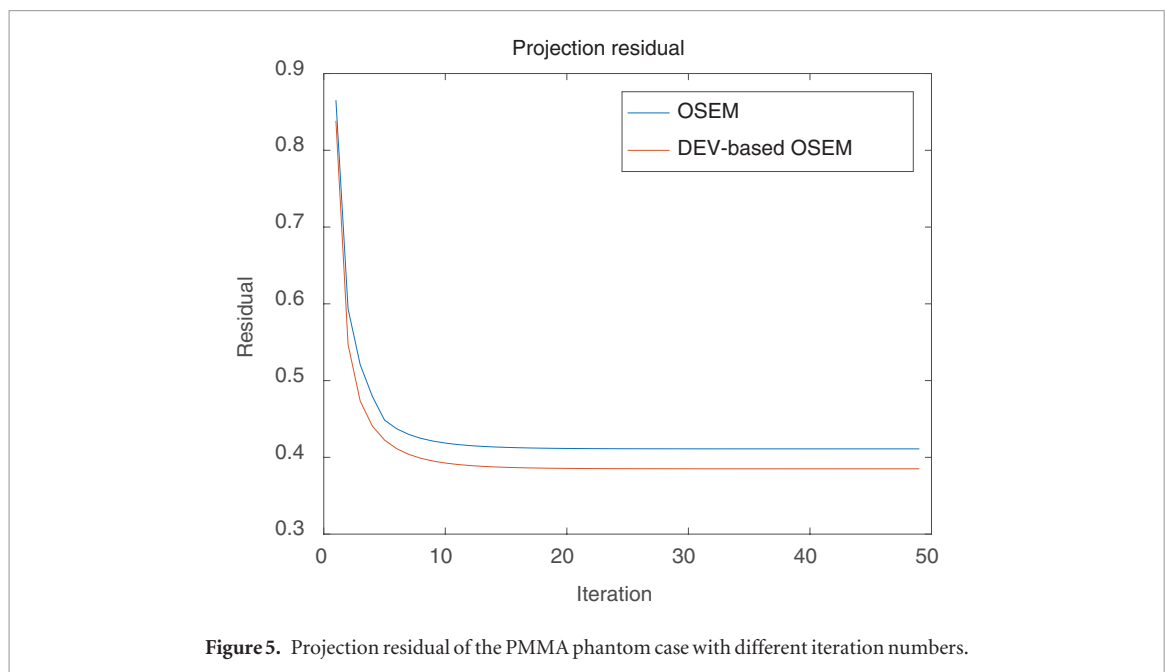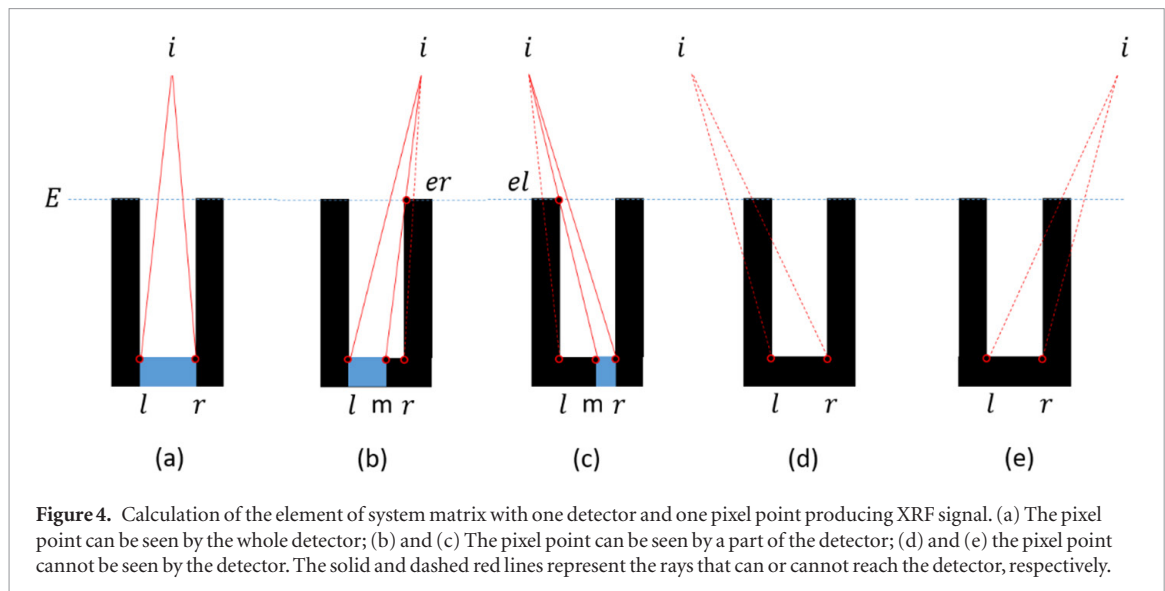
**Figure 3.** Comparison between (a) traditional and (b) DEV-based system matrix acquisitions. For an arbitrary pixel point $i$ within the object, XRF events are induced by external x-ray irradiation from the source (entering the object at point $a$), and XRF photons exit the object (exiting at point $C_{j-1}$, $C_j$, and $C_{j+1}$) and reach the detectors (point $j-1$, $j$, and $j+1$). $d_{i,j-1}$, $d_{i,j}$ and $d_{i,j+1}$ are widths of the detectors (point $j-1$, $j$, and $j+1$) that XRF signal from pixel point $i$ can reach, respectively. The red points are corresponding centers. For example, the following numerical values (based on the PMMA scan experimental setup) were used: $d_{i,j} = 1$ mm; the distance between $C_j$ and $j$ was 6 cm.

where $|ij|$ is the distance between point $i$ and $j$; $\mu_{beam}$ and $\mu_{gold}$ are the average attenuation coefficients of PMMA or biological tissues at the intensity-weighted mean energy of excitation beam and gold $K_\alpha$ XRF photon energies, respectively; $l_1$ is the segment of entering object point $a$ toward pixel point $i$; $l_{ij}$ is the segment of pixel point $i$ toward exiting object point $C_j$. $M_{i,j}$ is obtained by calculating the intersections between the collimator entrance (denoted as $E$ in figure 4) and the lines connecting the pixel point $i$ and the vertices at the collimator bottom (denoted as $l$ and $r$ in figure 4). The following possibilities can be considered: (1) if both intersections are at the collimator entrance (figure 4(a)), $d_{i,j}$ is equal to the collimator diameter; (2) if only the intersection between $E$ and $|il|$ is at the collimator entrance (figure 4(b)), calculate the intersection $m$ between the collimator bottom and the line connecting the pixel point $i$ to the collimator bottom through the inner right vertex of the collimator top (denoted as $er$ in figure 4(b)), and then $d_{i,j}$ is equal to the distance between $l$ and $m$; (3) if only the intersection between $E$ and $|ir|$ is at the collimator entrance (figure 4(c)), calculate the intersection $m$ between the collimator bottom and the line connecting the pixel point $i$ to the collimator bottom through the inner left vertex of the collimator top (denoted as $el$ in figure 4(c)), and then $d_{i,j}$ is equal to the distance between $r$ and $m$; (4) if neither of the intersections between $E$ and $|il|$ or $|ir|$ is at the collimator entrance (figures 4(d) and (e)), $d_{i,j}$ is equal to 0.

For comparison, FBP (inverse Radon transform, a built-in function of MATLAB), in conjunction with spline interpolation and a Ram-Lak filter, was also used for image reconstruction. For ease in visual comparison of reconstructed images, the pixel sizes of reconstructed PMMA phantom and mouse kidney images (0.25 mm × 0.25 mm and 0.75 mm × 0.75 mm, respectively) were matched among all three algorithms considered in this investigation.

As shown in figure 5, the projection residual ($\|Mf - p\|_2$) for the PMMA phantom case was calculated to determine the iteration numbers. Note $M$, $f$, and $p$ are as defined in equation (1). In all cases, the calculated residuals converged after 15 iterations. Thus, the iteration number of 15 was chosen for the PMMA phantom case in this study. Following the same process, the iteration number of 10 was chosen for the mouse kidney case.

## 2.3. Image analysis

For analysis of the spatial resolution, the FWHM was calculated as $2.355\sigma$ ($\sigma$ is the standard deviation of a fitting Gaussian function) (Schlueter *et al* 1994). The background noise in the reconstructed image, defined as the standard deviation of the pixel values outside the GNP-loaded regions, was also calculated for further analysis.

**Figure 4.** Calculation of the element of system matrix with one detector and one pixel point producing XRF signal. (a) The pixel point can be seen by the whole detector; (b) and (c) The pixel point can be seen by a part of the detector; (d) and (e) the pixel point cannot be seen by the detector. The solid and dashed red lines represent the rays that can or cannot reach the detector, respectively.



**Figure 5.** Projection residual of the PMMA phantom case with different iteration numbers.

## 3. Results

### 3.1. Comparison of reconstruction methods

For the purpose of comparison, FBP, traditional OSEM, and DEV-based OSEM were used for image reconstructions. Figure 6 shows the reconstructed images of the PMMA phantom and the mouse kidneys using the three reconstruction algorithms. FWHM and background noise values corresponding to the images are presented in figures 7 and 8, respectively. In the reconstructed image of the PMMA phantom, only the second and third columns were resolved by FBP and traditional OSEM, whereas all three columns were clearly resolved when the image was reconstructed by DEV-based OSEM. In the reconstructed image of the mouse kidneys, both kidneys were well separated by three algorithms. Figure 7 shows that the images reconstructed by DEV-based OSEM have smaller FWHM values than FBP and traditional OSEM, suggesting improvement in the image resolution (with respect to the reference images shown in figure 6). Images reconstructed by FBP contained more artifacts than traditional OSEM and DEV-based OSEM, as inferred from the results (background noise values) presented in figure 8. The background noise in the images reconstructed by FBP was up to an order of magnitude larger than traditional OSEM and DEV-based OSEM.
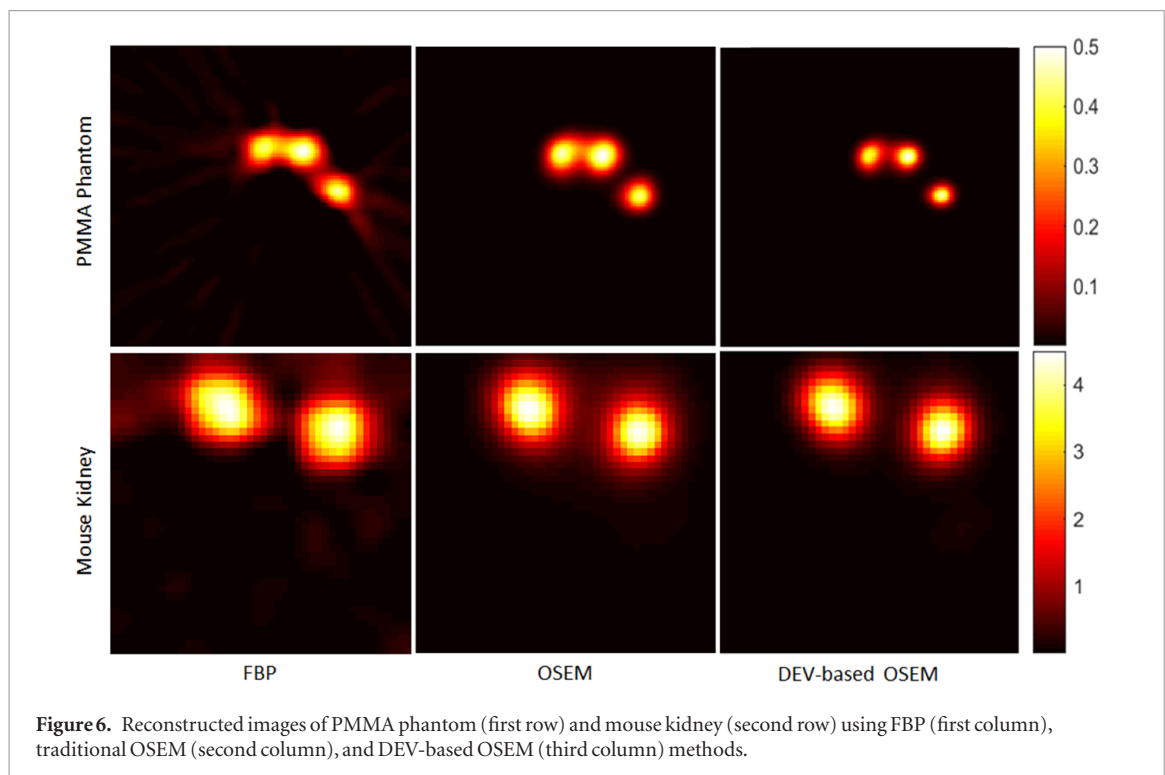
**Figure 6.** Reconstructed images of PMMA phantom (first row) and mouse kidney (second row) using FBP (first column), traditional OSEM (second column), and DEV-based OSEM (third column) methods.
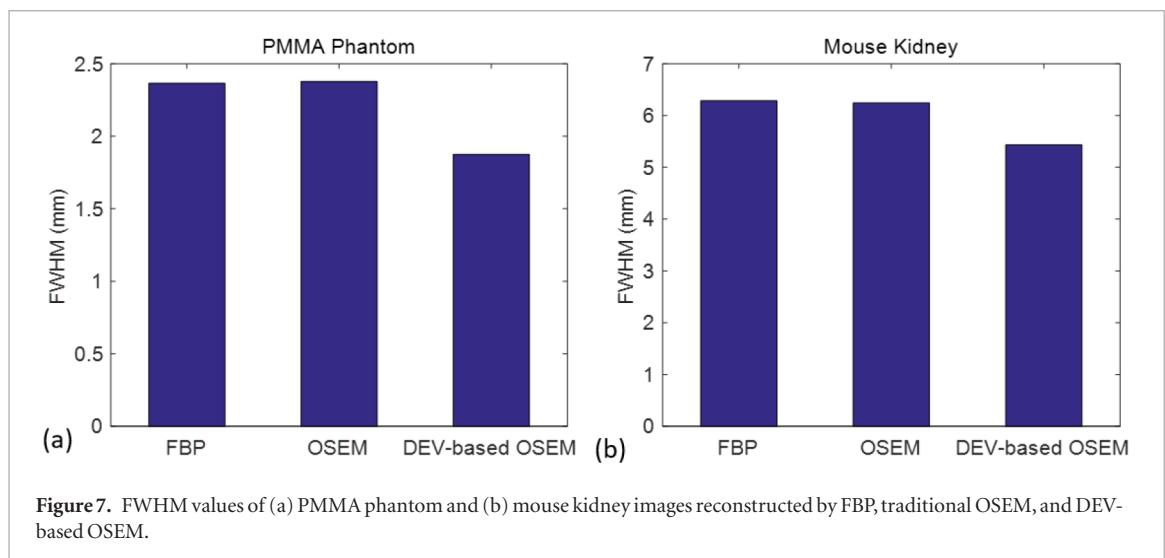


**Figure 7.** FWHM values of (a) PMMA phantom and (b) mouse kidney images reconstructed by FBP, traditional OSEM, and DEV-based OSEM.

## 4. Discussion

In this investigation, we have shown that DEV-based OSEM, which takes into account realistic DEV of XRF photons, results in improved image resolution, compared with FBP and traditional OSEM. To allow comparisons among these three algorithms, several factors were taken into consideration. For FBP, various filters (Hamming, Cosine, Ram-Lak, Shepp-Logan, and Hann) and interpolation methods (spline, linear, pchip, and nearest) were considered. Ram-Lak filter and spline interpolation were used in this study since they had better performance providing higher resolution than the rest. Also, the same image pixel sizes were used for all three algorithms, as explained earlier.

In principle, DEV-based OSEM can be used to improve XFCT image resolution when array or pixelated detectors are used in conjunction with parallel-hole collimators. Due to the absence of proper array or pixelated detector options, the majority of benchtop XFCT-related investigations have been conducted with a single crystal detector with a pin-hole type collimator. In previous studies, therefore, the detector needed to be translated multiple times (e.g. along the incident beam direction) to acquire XRF signals from the entire imaging object. Accordingly, any effects dependent on DEV (i.e. solid angle subtended by the detector at a pixel point through the detector collimator aperture) at the neighboring detector positions were not properly investigated. Mean-
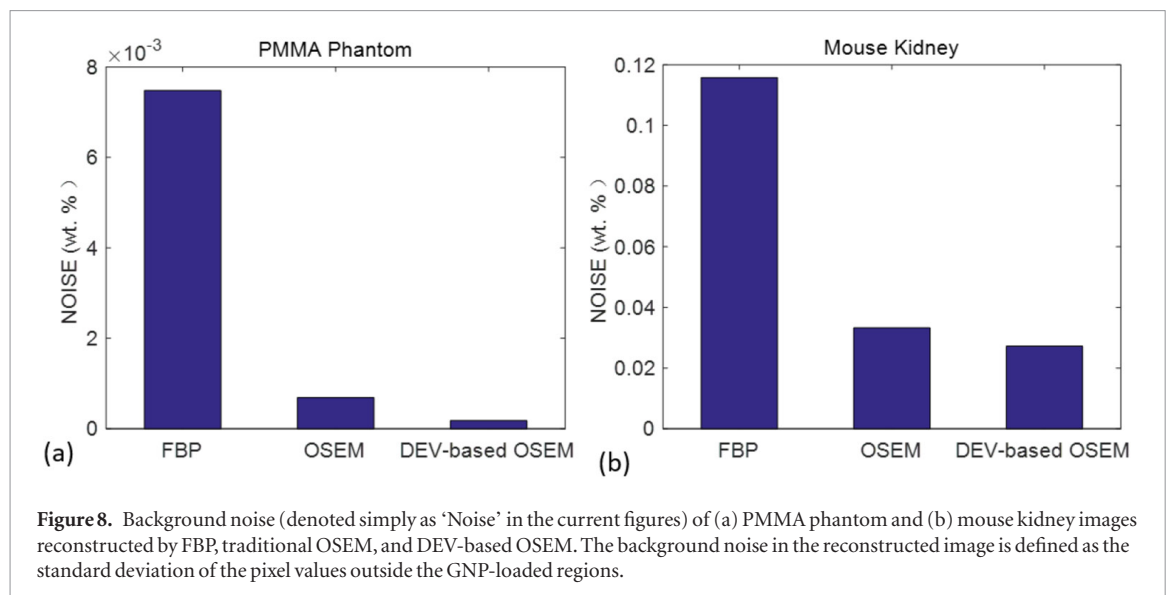
**Figure 8.** Background noise (denoted simply as 'Noise' in the current figures) of (a) PMMA phantom and (b) mouse kidney images reconstructed by FBP, traditional OSEM, and DEV-based OSEM. The background noise in the reconstructed image is defined as the standard deviation of the pixel values outside the GNP-loaded regions.

while, there is growing interest in deploying array or pixelated detectors into benchtop XFCT setups in order to accomplish routine *in vivo* imaging of small animals under realistic constrains of x-ray dose and scan time (Jones and Cho 2011, Manohar *et al* 2016). If XRF signals are acquired using array or pixelated detectors (coupled with parallel-hole collimation), DEV-related effects will no longer be negligible during XFCT image reconstruction. In this regard, approaches such as DEV-based OSEM will be found particularly useful, in terms of further improving XFCT image resolution. Further adaptation and investigation of DEV-based OSEM, while taking into account various detector collimator designs, will also be necessary.

There are a number of limitations to the currently proposed algorithm such as computational cost. Iterative algorithms (traditional and DEV-based OSEMs) took longer to perform the reconstruction than FBP, and DEV-based OSEM required more calculation and reconstruction time than traditional OSEM. Image reconstructions were implemented in MATLAB R2014b on a computer with the Intel Core i5-4590 CPU running at 3.30 GHz, RAM running at 8.00 GB, and a 64-bit operating system. FBP took less than 1 s for both mouse and PMMA phantom data. For 30 projections and 11 steps, traditional OSEM took 2 s and DEV-based OSEM took 47 s; for 60 projections and 30 steps, traditional OSEM took 20 s and DEV-based OSEM took 664 s. Moreover, OSEM requires system information, which might be different among the XFCT setups. Although considerable at the moment, these limitations will likely diminish with future developments and updates of the XFCT setups.

## 5. Conclusion

In the current study, data derived from benchtop XFCT scanning of a custom-made PMMA phantom and a tumor-bearing mouse were used to validate the proposed DEV-based OSEM algorithm for benchtop XFCT image reconstruction. DEV-based OSEM, which considered DEV of a parallel-hole collimator, resulted in higher spatial resolution (lower FWHM) and lower background noise than FBP or traditional OSEM. Overall, the current investigation provided a more effective method for benchtop XFCT image reconstruction, which can propel further advancement of benchtop XFCT imaging techniques.

## Acknowledgments

# References

Cesareo R and Mascarenhas S 1989 A new tomographic device based on the detection of fluorescent x-rays *Nucl. Instrum. Methods Phys. Res.* A **277** 669–72

Cesareo R and Viezzoli G 1983 Trace element analysis in biological samples by using XRF spectrometry with secondary radiation *Phys. Med. Biol.* **28** 1209

Cheong S K, Jones B L, Siddiqi A K, Liu F, Manohar N and Cho S H 2010 X-ray fluorescence computed tomography (XFCT) imaging of gold nanoparticle-loaded objects using 110 kVp x-rays *Phys. Med. Biol.* **55** 647–62

Hsieh J 2003 *Computed Tomography: Principles, Design, Artifacts, and Recent Advances* vol 114 (Bellingham, WA: SPIE Optical Engineering Press)

Hudson H M and Larkin R S 1994 Accelerated image reconstruction using ordered subsets of projection data *IEEE Trans. Med. Imaging* **13** 601–9

Jones B L and Cho S H 2011 The feasibility of polychromatic cone-beam x-ray fluorescence computed tomography (XFCT) imaging of gold nanoparticle-loaded objects: a Monte Carlo study *Phys. Med. Biol.* **56** 3719–30

Jones B L, Manohar N, Reynoso F, Karellas A and Cho S H 2012 Experimental demonstration of benchtop x-ray fluorescence computed tomography (XFCT) of gold nanoparticle-loaded objects using lead- and tin-filtered polychromatic cone-beams *Phys. Med. Biol.* **57** N457–67

Kak A C and Slaney M 1988 *Principles of Computerized Tomographic Imaging* (New York: IEEE)

Kuang Y, Pratx G, Bazalova M, Meng B, Qian J and Xing L 2013 First demonstration of multiplexed x-ray fluorescence computed tomography (XFCT) imaging *IEEE Trans. Med. Imag.* **32** 262–7

Lange K and Carson R 1984 EM reconstruction algorithms for emission and transmission tomography *J. Comput. Assist. Tomogr.* **8** 306–16

Manohar N, Reynoso F J and Cho S H 2018 Technical note: a benchtop cone-beam x-ray fluorescence computed tomography (XFCT) system with a high-power x-ray source and transmission CT imaging capability *Med. Phys.* **45** 4652–9

Manohar N, Reynoso F J, Diagaradjane P, Krishnan S and Cho S H 2016 Quantitative imaging of gold nanoparticle distribution in a tumor-bearing mouse using benchtop x-ray fluorescence computed tomography *Sci. Rep.* **6** 22079

Pushie M J, Pickering I J, Korbas M, Hackett M J and George G N 2014 Elemental and chemically specific x-ray fluorescence imaging of biological systems *Chem. Rev.* **114** 8499–541

Rust G-F and Weigelt J 1998 X-ray fluorescent computer tomography with synchrotron radiation *IEEE Trans. Nucl. Sci.* **45** 75–88

Schlueter F J, Wang G, Hsieh P S, Brink J A, Balfe D M and Vannier M W 1994 Longitudinal image deblurring in spiral CT *Radiology* **193** 413–8

Shepp L A and Vardi Y 1982 Maximum likelihood reconstruction for emission tomography *IEEE Trans. Med. Imaging* **1** 113–22